

Flowfield Simulations in Industrial Furnace Configurations

Paul A. Gillis and Philip J. Smith

Combustion Computations Laboratory
75 CTB, Brigham Young University
Provo, Utah 84604

1 Introduction

A fundamental element of comprehensive pulverized-fuel combustion modelling is the description of the turbulent gaseous flow field within the furnace. As part of a program to develop a three-dimensional coal combustion code, a non-reacting gas flow dynamics model has been developed. This flow model, GAS3D, has been demonstrated in a variety of industrial configurations including corner-fired, cross-fired, and wall-fired furnace geometries. This paper discusses the components and capabilities of the model and presents comparisons between experimental data and model predictions for a wall-fired furnace.

The emphasis of this paper is on evaluating model performance. Experimental data has been obtained from Consolidation Coal Company for a wall-fired furnace. This configuration has been simulated with GAS3D using three different turbulence models. A description of the flow patterns predicted within the furnace are given. Comparisons are made between the predictions and experimental data and between the different turbulence models.

2 Solution Method

Steps common to all finite difference numerical techniques are the formulation of the equations, discretization of these equations, and the solution of the resulting coefficient matrices. GAS3D couples the momentum and continuity equations with the SIMPLE algorithm (1), utilizes a first-order hybrid upwind and central differencing scheme, and iteratively solves the difference coefficient matrices by approximating them as tridiagonal systems, which are solved with the Thomas algorithm.

The SIMPLE (Semi-Implicit Method for solving Pressure Linked Equations) algorithm is a technique for solving the equations of motion and continuity in a decoupled fashion. It requires a initial guess of the pressure field which is then updated through the calculation of a pressure correction. This method of solving the pressure field can require hundreds of iterations and alternative numerical techniques are being investigated. These alternatives include solving the equations in a coupled manner, similar to Vanka's BLIMM method (2) and the use of multigrid algorithms (3).

Finite difference coefficient matrices are often very sparse and the direct inversion of these matrices is rarely practical. Due to the first-order differencing of convection terms employed in GAS3D, the matrices formed are heptadiagonal. Each matrix is first approximated as a series of three tridiagonal matrices. These tridiagonal matrices are then solved individually with the Thomas algorithm and the solution procedure is repeated several times to resolve the coupling in the three coordinate directions. This matrix solver was initially observed to account for up to 65% of the overall run time on a CONVEX C-1 computer. Reordering the inner loops of the Thomas algorithm eliminated recursion and allowed for vectorization of the solver. This resulted in a significant reduction in matrix solution (~ 80 %) and overall computational (~ 40 %) time.

3 Model Capabilities

The model allows for simulations to be made in either the Cartesian or polar coordinate system. Initial validation of the model was made through comparisons with the predictions from an extensively evaluated axisymmetric gas dynamics code (4). A case was first run and documented with the axisymmetric model. This axisymmetric geometry was input and flow was simulated with the three-dimensional model for both coordinate systems. Predictions from the 3-D polar case were indistinguishable from the axisymmetric run. Cartesian predictions were similarly validated through comparison.

GAS3D has been written in a modular manner to aid understanding and ease modification. The model consists of a main driver and forty-four subroutines, each made up of an average of 134 lines of FORTRAN coding. All boundary conditions are controlled by a single three-dimensional array which specifies each cell (computational node) as being part of an inlet, flow field, or a wall (intrusion). Complex geometries can be easily simulated by input to this geometry array. Thus, a preprocessor can prepare this array for model input. Inlet velocity profiles, including swirling burners, can also be input directly to the code. Inlets and outlets on all six faces of the computational domain are possible through the same array. There is no limitation to the number of inlets or outlets on any one face, nor the number of faces having inlets, outlets, or both. However, if an outlet is located within a recirculation zone, an overall mass balance cannot be adequately closed and the code will not fully converge. The model will also handle structural intrusions at any point in the flow field. Intrusions are needed to model such important features as inlet quarls, ash bins, tube banks, clipped corners, and the furnace nose. Test cases have been successfully converged which included constricted exits, flow around successive baffles, and bluff bodies surrounded on all six sides by the flow field.

4 Turbulence Models

The differential equation set employed in the model was derived from the vector forms of the conservation equations for mass and momentum (5). The equations were manipulated into a standard steady-state form to ease differencing. The instantaneous form of the expanded conservation equations were Favre averaged to allow for a computationally feasible length scales:

$$\bar{\phi} \equiv \frac{\overline{\rho\phi}}{\bar{\rho}} \quad (1)$$

The Reynold's stresses, $\rho\overline{u_i u_j}$, where u_i is the fluctuating component of velocity in the i th direction, are modelled with the Boussinesq hypotheses:

$$-\overline{u_i u_j} = -\mu_t \nabla \bar{u} \quad (2)$$

The time averaged differential equations can be manipulated to resemble the instantaneous form of the equations by combining the molecular viscosity, μ_t , with the eddy diffusivity. This differential equation set, for both the Cartesian and cylindrical coordinate systems, is presented in its Favre averaged form in Table 1.

Turbulence closure models have been developed for varying levels of sophistication. The most basic models, such as the constant eddy diffusivity model and Prandtl's mixing length model, contain simplifications which normally restrict their application. The most commonly used turbulence model is the two-equation $k-\epsilon$ model. Its popularity is due in part to the disadvantages of its more sophisticated alternatives, namely, second-order closure models and large-eddy simulations. These alternatives are hindered by the enormous increase in computational resources

needed to either solve the Reynolds stress transport equations in second-order closures or resolve the fine time and spacial scales required for large-eddy simulations.

The simplest turbulence assumption is that of constant eddy diffusivity. Because turbulence is normally generated due to shear forces in the gases, this assumption is rarely true. The a priori determination of an average eddy diffusivity is difficult. A slightly more sophisticated closure scheme is the Prandtl's mixing length model. This model, given by Equation 3, relates the eddy diffusivity to the mean velocity gradient.

$$\mu_t = \rho l_m^2 |\nabla \bar{u}| \quad 3)$$

The main drawback with this model is the determination of the mixing length, l_m , for complex flows. The value for l_m has been empirically determined for a number of simple jets and flows but a value of l_m for recirculating and three-dimensional flows is difficult to determine.

The k- ϵ turbulence model was introduced to provide a means of modeling the transport of k, the turbulent kinetic energy, and ϵ , the dissipation of turbulent kinetic energy. Transport equations are devised for both k and ϵ that include terms to model convection, diffusion, production, and dissipation of these quantities. The differential equations for k and ϵ , including the generation term, G, used in the model are given in Table 1. These equations are solved for each gas phase iteration. After obtaining local values for k and ϵ , the local eddy diffusivity is calculated from the Prandtl-Kolmogorov relationship:

$$\mu_t = \frac{C_\mu \rho k^2}{\epsilon}, C_\mu = 0.09 \quad 4)$$

GAS3D currently contains options for the use of a constant eddy diffusivity, the Prandtl's mixing length turbulence model, or the standard k- ϵ model.

5 Reactor Flow Patterns

The pilot scale furnace simulated in this paper is operated by Consolidation Coal Corporation in Liberty, Pennsylvania. The furnace is approximately $\frac{1}{10}$ scale of a full utility boiler and is fired from four swirled burners. The burners are located on a single wall in a diamond configuration and are all swirled in the same direction. The outlet is located above the burners on the east wall. Details about the furnace configuration can be seen in Figures 1 and 2. The furnace geometry is similar in design to large industrial boilers and contains an ash bin, furnace nose, and several clipped corners. This geometry was modelled with a grid that contained 35 points in the x or depth direction, 45 points in the y or width direction, and 65 points in the z or height direction. Converged results for this 102375 node case were obtained using the three turbulence models described previously. Each turbulence model produced significantly differing results.

The constant eddy diffusivity model produced the simplest flow field. This flow field contained only two large scale vortices. The largest vortex was predominantly visible in the x planes, flowed in the clockwise direction, and extended over the entire length of the reactor. No large recirculation zones were predicted in the z planes, but burner centerline recirculation was present. Figure 1A illustrates flow patterns at a normalized width of 0.5. This figure shows a strong vortex centered below the burners that extends approximately half way up the reactor. The shaded areas in these figures represent reactor walls and the arrows signify velocity vectors constructed from the two components of velocity parallel to the designated plane. The length and direction of each vector represents predicted velocity for the location specified by the vector tail. In order to reduce congestion, less than one half of the computational nodes are represented with vectors. There are

two sizes of unfilled arrowheads and their ratio along with the scale for the small vectors is given in Figures 1 and 2.

Figure 1B provides the flow field prediction for the center y plane using a mixing length turbulence model. This figure shows a highly viscous type flow, especially in the near-burner region and the absent of major vortices in this plane. The viscous flow is generated because the mixing length model produces high eddy diffusivity values in the high velocity gradient regions around the burners. The x plane predictions show high velocities along the north wall which decrease to near stagnation along the south wall. Strong counter-clockwise swirling vortices are found in all the z planes starting in the ash bin and extending beyond the furnace nose.

The $k-\epsilon$ turbulence model yielded the most complex flow field prediction. Figure 1C reveals numerous swirling patterns in this single plane. Separate vortices in the ash bin, above the burners, and behind each burner, as well as strong burner centerline recirculations are all predicted. Clockwise swirling vortices are observed in nearly all the z planes. Numerous localized vortices can be found in the predicted x planes. The $k-\epsilon$ turbulence model predicted a central recirculation zone with gases flowing downward in the center of the reactor, but flowing upward near the east, west, north and south walls. Figure 1 illustrates the vast differences in both magnitude and direction of the velocities predicted by the three turbulence models.

6 Data Comparisons

Velocity measurements in the Consol furnace were made with a $\frac{1}{4}$ inch pitot tube connected to an electro-manometer. The y component of velocity was not included in these measurements. Experimental velocity data were obtained for 50 points all above the burners. The filled arrowheads in Figures 1 and 2 represent these data points. In Figure 2, all 50 data points are shown with the $k-\epsilon$ predictions. It should be noted in Figure 2 that the data points are for the vertical component of velocity only.

The predictions in Figure 1C agree significantly better than the predictions of Figures 1A or 1C. The agreement between predictions and data in Figures 1A and 1B is poor. For example, the $k-\epsilon$ simulation is the only model that predicted downward flow in the reactor center and higher velocities on east wall than on the west wall. The majority of experimental vectors in Figure 1C agree with the predictions in both direction and magnitude. The obvious exceptions are the center data vectors at a normalized height of 0.58 and 0.70. There are several possible reasons for these discrepancies. The most probable cause is that the central recirculation zone is being overpredicted by the $k-\epsilon$ model. An earlier study on two-dimensional swirling flows faulted the $k-\epsilon$ model with overpredicting the length of recirculation zones (6). The transient nature of turbulence could create difficulties in correcting determining direction and magnitude of gas velocity in a recirculation zone. The steady-state velocity predicted by GAS3D could be difficult to verify in a region where turbulent eddies are constantly passing. More precise inlet conditions could also aid isolated the cause of these discrepancies.

Figures 2 shows predicted flowfields at three different depths: Figure 2A represents a x plane near the burners and east wall; Figure 2B represents a x plane at a normalized depth of 0.5; and Figure 2C is near the west wall. The swirl in the secondary of the burners drives the lower clockwise vortices found in Figures 2A and 2B. A counter clockwise swirling pattern can also be found in outlet in the upper part of Figures 2A and 2B. Although not always exact in magnitude, the $k-\epsilon$ model appears to predict the trends shown by the data. In Figure 2A, the model predicted the change from higher north wall velocities to higher south wall velocities as the gases flowed upward. The two data points in direct directional disagreement with predictions seen in Figure 1C can also be found in Figure 2B. It is probable that if the central recirculation zone length

could be better simulated the agreement in the top data plane (height = 0.70) would improve. The general agreement illustrated in Figures 1C, 2A, 2B, and 2C is reasonable considering the complexity of the flow.

The presence of a fine vortex structure in the $k-\epsilon$ predictions presents some interesting questions. Additional work is needed to determine the dependence of vortex structure on coarseness of the grid. Additional vortex structure could be revealed by converging this case with finer grid sizing. Previous investigators have found that the inlet conditions are vital to correctly simulating turbulent flow. Further investigation is warranted into determining the sensitivity of solutions to such parameters as swirl number and inlet velocity profile.

7 Conclusion

A three-dimensional flow model has been developed and validated for simulating complex enclosed flow. The selection of turbulence model has been shown to greatly affect flow predictions. The $k-\epsilon$ model appeared to represent significant predictive improvement over the simpler turbulence models. Although the $k-\epsilon$ model appeared to overpredict the size of some recirculation zones, it yielded predictions in general agreement with experimental data. Further study is warranted to determine the applicability of other turbulence models and the effect of grid resolution and inlet conditions on predictions.

8 Acknowledgements

We wish to thank Consolidation Coal Corporation for providing the experimental data used in this paper. Additional support for this research was provided by the following organizations: Advanced Fuel Resources, Inc., Babcock and Wilcox, Combustion Engineering, Inc., Consolidation Coal Company, Electric Power Research Institute, Empire State Electric Energy Research Co., Foster Wheeler Development Co., Tennessee Valley Authority, U.S. Department of Energy - METC, U.S. Department of Energy - PETC, and Utah Power and Light Co.

9 References

1. Patankar, S.V., Numerical Heat Transfer and Fluid Flow, McGraw-Hill Book Company, New York (1980).
2. Vanka, S.P., "Block-Implicit Multigrid Solution of Navier-Stokes Equations in Primitive Variables," Journal of Computational Physics, Vol. 65, 138-158 (1986).
3. Brandt, A., Multigrid Techniques: 1984 Guide with Applications to Fluid Dynamics, GMD-Studien Nr. 85, Schloss Birlinghoven, West Germany (1984).
4. Smoot, L.D. and Smith, P.J., Coal Combustion and Gasification, Plenum Press, New York (1985).
5. Bird, R.B., Stewart, W.E., and Lightfoot, E.N., Transport Phenomena, John Wiley & Sons, New York (1960).
6. Sloan, D.G., Smith, P.J., and Smoot, L.D., "Modeling of Swirl in Turbulent Flow Systems," Prog. Energy Combust. Sci., Vol. 12, 163-250 (1986).

Table 1. Differential Equation Set for GAS3D

Part A. Cartesian Coordinate System

$$\frac{\partial(\bar{\rho}\tilde{u}\phi)}{\partial x} + \frac{\partial(\bar{\rho}\tilde{v}\phi)}{\partial y} + \frac{\partial(\bar{\rho}\tilde{w}\phi)}{\partial z} - \frac{\partial}{\partial x} \left(\Gamma_{\phi} \frac{\partial\phi}{\partial x} \right) - \frac{\partial}{\partial y} \left(\Gamma_{\phi} \frac{\partial\phi}{\partial y} \right) - \frac{\partial}{\partial z} \left(\Gamma_{\phi} \frac{\partial\phi}{\partial z} \right) = S_{\phi}$$

Equation	ϕ	Γ_{ϕ}	S_{ϕ}
Continuity	1	0	0
X Momentum	\tilde{u}	μ_e	$-\frac{\partial P}{\partial x} + \frac{\partial}{\partial x} \left(\mu_e \frac{\partial \tilde{u}}{\partial x} \right) + \frac{\partial}{\partial y} \left(\mu_e \frac{\partial \tilde{u}}{\partial x} \right) + \frac{\partial}{\partial z} \left(\mu_e \frac{\partial \tilde{u}}{\partial x} \right)$
Y Momentum	\tilde{v}	μ_e	$-\frac{\partial P}{\partial y} + \frac{\partial}{\partial x} \left(\mu_e \frac{\partial \tilde{u}}{\partial y} \right) + \frac{\partial}{\partial y} \left(\mu_e \frac{\partial \tilde{u}}{\partial y} \right) + \frac{\partial}{\partial z} \left(\mu_e \frac{\partial \tilde{u}}{\partial y} \right)$
Z Momentum	\tilde{w}	μ_e	$-\frac{\partial P}{\partial z} + \frac{\partial}{\partial x} \left(\mu_e \frac{\partial \tilde{u}}{\partial z} \right) + \frac{\partial}{\partial y} \left(\mu_e \frac{\partial \tilde{u}}{\partial z} \right) + \frac{\partial}{\partial z} \left(\mu_e \frac{\partial \tilde{u}}{\partial z} \right)$
Turbulent Energy	k	$\frac{\mu_e}{\sigma_k}$	$G - \bar{\rho}\epsilon$
Dissipation Rate	ϵ	$\frac{\mu_e}{\sigma_{\epsilon}}$	$\left(\frac{\epsilon}{k} \right) (c_1 G - c_2 \bar{\rho}\epsilon)$

where:

$$G = \mu_e \left\{ 2 \left[\left(\frac{\partial \tilde{u}}{\partial x} \right)^2 + \left(\frac{\partial \tilde{u}}{\partial y} \right)^2 + \left(\frac{\partial \tilde{u}}{\partial z} \right)^2 \right] + \left(\frac{\partial \tilde{u}}{\partial y} + \frac{\partial \tilde{v}}{\partial x} \right)^2 + \left(\frac{\partial \tilde{u}}{\partial z} + \frac{\partial \tilde{w}}{\partial x} \right)^2 + \left(\frac{\partial \tilde{v}}{\partial z} + \frac{\partial \tilde{w}}{\partial y} \right)^2 \right\}$$

Part B. Cylindrical Coordinate System

$$r \frac{\partial(\bar{\rho}\tilde{u}\phi)}{\partial x} + \frac{\partial(\bar{\rho}\tilde{v}\phi)}{\partial r} + \frac{\partial(\bar{\rho}\tilde{w}\phi)}{\partial \theta} - r \frac{\partial}{\partial x} \left(\Gamma_{\phi} \frac{\partial\phi}{\partial x} \right) - \frac{\partial}{\partial r} \left(r \Gamma_{\phi} \frac{\partial\phi}{\partial r} \right) - \frac{\partial}{\partial \theta} \left(\frac{\Gamma_{\phi}}{r} \frac{\partial\phi}{\partial \theta} \right) = S_{\phi}$$

Equation	ϕ	Γ_{ϕ}	S_{ϕ}
Continuity	1	0	0
X Momentum	\tilde{u}	μ_e	$-r \frac{\partial P}{\partial x} + r \frac{\partial}{\partial x} \left(\mu_e \frac{\partial \tilde{u}}{\partial x} \right) + \frac{\partial}{\partial r} \left(\mu_e r \frac{\partial \tilde{u}}{\partial x} \right) + \frac{\partial}{\partial \theta} \left(\mu_e \frac{\partial \tilde{u}}{\partial x} \right)$
R Momentum	\tilde{v}	μ_e	$-r \frac{\partial P}{\partial r} + r \frac{\partial}{\partial x} \left(\mu_e \frac{\partial \tilde{u}}{\partial r} \right) + \frac{\partial}{\partial r} \left(\mu_e r \frac{\partial \tilde{u}}{\partial r} \right) + \frac{\partial}{\partial \theta} \left(\mu_e \frac{\partial \tilde{u}}{\partial r} - \frac{\tilde{w}}{r} \right) - \frac{2\mu_e}{r} \frac{\partial \tilde{w}}{\partial \theta} - \frac{2\tilde{u}\mu_e}{r} + \bar{\rho}\tilde{w}^2$
θ Momentum	\tilde{w}	μ_e	$-\frac{\partial P}{\partial \theta} + r \frac{\partial}{\partial x} \left(\mu_e \frac{\partial \tilde{u}}{\partial \theta} \right) + \frac{\partial}{\partial r} \left(\mu_e \frac{\partial \tilde{u}}{\partial \theta} - \mu_e \tilde{w} \right) + \frac{\partial}{\partial \theta} \left[\left(\frac{\mu_e}{r} \right) \left(\frac{\partial \tilde{w}}{\partial \theta} + 2r \frac{\tilde{v}}{\partial r} \right) \right] + \mu_e \left(\frac{\partial \tilde{w}}{\partial r} + \frac{\partial \tilde{v}}{r \partial \theta} - \frac{\tilde{w}}{r} \right) - \bar{\rho}\tilde{v}\tilde{w}$
Turbulent Energy	k	$\frac{\mu_e}{\sigma_k}$	$r(G - \bar{\rho}\epsilon)$
Dissipation Rate	ϵ	$\frac{\mu_e}{\sigma_{\epsilon}}$	$\left(r \frac{\epsilon}{k} \right) (c_1 G - c_2 \bar{\rho}\epsilon)$

where:

$$G = \mu_e \left\{ 2 \left[\left(\frac{\partial \tilde{u}}{\partial x} \right)^2 + \left(\frac{\partial \tilde{v}}{\partial r} \right)^2 + \left(\frac{\partial \tilde{w}}{r \partial \theta} + \frac{\tilde{v}}{r} \right)^2 \right] + \left(\frac{\partial \tilde{u}}{\partial r} + \frac{\partial \tilde{v}}{\partial x} \right)^2 + \left(\frac{\partial \tilde{u}}{r \partial \theta} + \frac{\partial \tilde{w}}{\partial x} \right)^2 + \left(\frac{\partial \tilde{v}}{r \partial \theta} + \frac{\partial \tilde{w}}{r^2} \right)^2 \right\}$$

U-W Velocity Vectors

Large to Small Vector Length Ratio = 20
Velocity Scale: 1 inch = 1.44 m/s

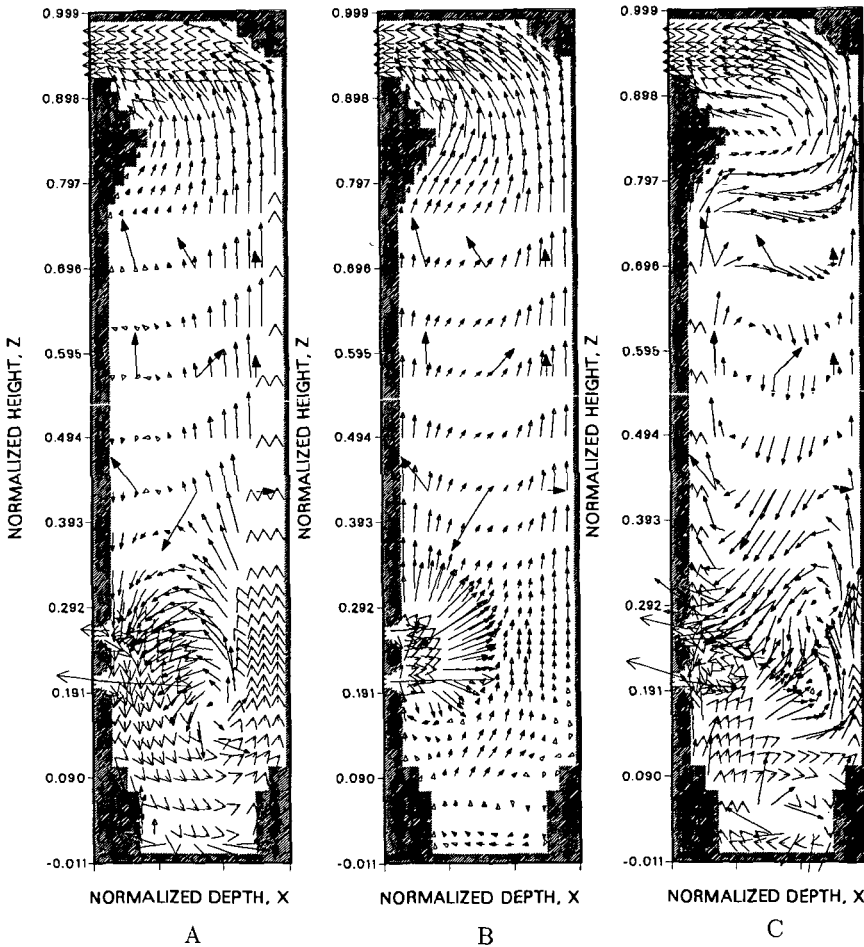


Figure 1. Comparison of velocity predictions and experimental data at a normalized width of 0.5 for the following turbulence models: A, constant eddy diffusivity; B, simple mixing length model; and C, $k-\epsilon$ model.

V-W Velocity Vectors

Large to Small Vector Length Ratio = 20
Velocity Scale: 1 inch = 1.44 m/s

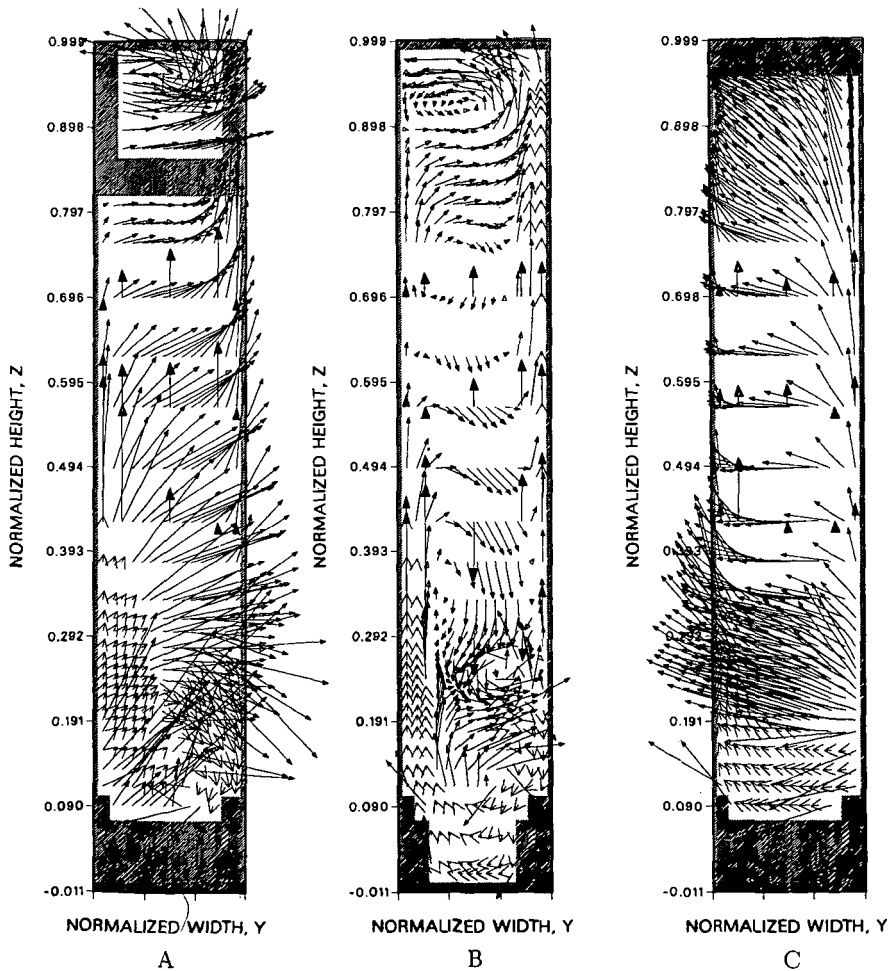


Figure 2. Comparison of velocity predictions and the vertical component of velocity measured in three x planes: A, normalized depth of 0.17; B, normalized depth of 0.50; C, normalized depth of 0.83.